

Scale-Consistent Fusion: from Heterogeneous Local Sampling to Global Immersive Rendering

Wenpeng Xing, Jie Chen, Zaifeng Yang and Qiang Wang

Abstract—Image-based geometric modeling and novel view synthesis based on sparse, large-baseline samplings are challenging but important tasks for emerging multimedia applications such as virtual reality and immersive telepresence. Existing methods fail to produce satisfactory results due to the limitation on inferring reliable depth information over such challenging reference conditions. With the popularization of commercial light field (LF) cameras, capturing LF images (LFIs) is as convenient as taking regular photos, and geometry information can be reliably inferred. This inspires us to use a sparse set of LF captures to render high-quality novel views globally. However, fusion of LF captures from multiple angles is challenging due to the scale inconsistency caused by various capture settings. To overcome this challenge, we propose a novel scale-consistent volume rescaling algorithm that robustly aligns the disparity probability volumes (DPV) among different captures for scale-consistent global geometry fusion. Based on the fused DPV projected to the target camera frustum, novel learning-based modules have been proposed (i.e., the attention-guided multi-scale residual fusion module, and the disparity field guided deep re-regularization module) which comprehensively regularize noisy observations from heterogeneous captures for high-quality rendering of novel LFIs. Both quantitative and qualitative experiments over the Stanford Lytro Multi-view LF dataset show that the proposed method outperforms state-of-the-art methods significantly under different experiment settings for disparity inference and LF synthesis.

Index Terms—Novel view synthesis, light field, disparity probability volumes rescaling, spatial-angular re-regularization, multi-scale residual fusion.

I. INTRODUCTION

REPRODUCING photorealistic appearance of visual contents is one of the core tasks for computer graphics and computer vision. Existing approaches fall into two major categories: physically based rendering (PBR) and image-based rendering (IBR). PBR focuses on faithful modeling of light propagation and its interactions with the environment. IBR, in contrast, works directly on images captured under real settings and renders novel views based on estimated geometry with operations such as warping and blending [1], [2]. IBR is computationally much more efficient than PBR, but its quality depends heavily on the source view’s sampling pattern and the reconstruction algorithm. In this work, we will focus on a novel globally sparse, but locally dense sampling and fusion mechanism for high-quality and scale-consistent IBR.

W. Xing, J. Chen (correspondence author) and Q. Wang are with the Department of Computer Science, Hong Kong Baptist University, Hong Kong. E-mails: {cswpxing, chenjie and qiangwang}@comp.hkbu.edu.hk. Z. Yang is with the Department of Electronics and Photonics, Institute of High Performance Computing, A*STAR, Singapore. E-mail: yang_zweifeng@ihpc.a-star.edu.sg.

Recent years have witnessed blooming studies on IBR which apply deep learning techniques to boost the performance in both geometry inference and novel view synthesis. Various methods have been developed that model the 3D scene contents with different forms of representations, i.e., layered depth images [3], multi-plane images (MPI) [2], [4], point clouds [5], and voxels [6]. These representations show limitations on synthesizing complex scenes with arbitrary sampling patterns. Neural rendering methods avoid explicit modeling of the scene geometry and directly synthesize pixels with a generative network, e.g., the DeepVoxels [7] and the neural radiance fields [8]. These models require dense sampling of a compact target area and are not scalable for other large scenes. Multi-view stereo systems [9], [10] also work poorly over sparse inputs as they rely on continuous cost volumes for efficient geometry inference, which is both theoretically and computationally challenging with sparse source inputs.

Image-based geometric modeling and view synthesis based on *sparse, large-baseline* samplings are challenging but important tasks for emerging multimedia applications such as virtual reality and immersive telepresence. Existing methods fail to produce satisfactory results due to the limitation on inferring reliable depth information over such challenging reference conditions. With the popularization of commercial light field (LF) cameras like Lytro [11] and Raytrix [12], capturing LF images is as convenient as taking regular photos, and geometry information can be reliably inferred. With locally dense sampling of the target scene, reliable disparity could be estimated. This inspires us to use a sparse set of LF captures to globally render high-quality novel views, which not only reduces the requirement for dense global sampling to a sparse set of locally dense angular sampling by the LF, but also enables us to deal with more dynamic scenes as only a few shots are required.

Fusion of LF captures from multiple angles is challenging due to the scale inconsistency caused by varying focal settings between different captures. To overcome this challenge, we propose a novel Scale-Consistent Volume Rescaling (SCVR) algorithm which robustly aligns the disparity planes of Disparity Probability Volumes (DPV) among views for a consistent fusion. This rescaling process enables natural adaptation to various camera configurations and fuses the heterogeneous samplings into a globally consistent geometry embedding. Based on the fused DPV projected to a target camera view, a disparity map is synthesized and refined with the target RGB capture as a guide. The LF at the novel view is subsequently synthesized and deeply regularized based on the disparity field. The synthesized LF is aligned to the direction and capture

settings of the target view (including focal length, exposure, resolution, etc.). We can consequently achieve robust rendering for any heterogeneous target imagery, achieving our goal of global immersive rendering. Both quantitative and qualitative experiments over the Stanford Lytro Multi-view LF dataset show that the proposed method outperforms state-of-the-art methods under different experiment settings, for both disparity inference and LF Synthesis. The contributions of this paper can be generalized as:

- We have proposed an integrated immersive content capture scheme which can transfer the requirement of globally-dense sampling to a sparse set of locally-dense sampling (in the forms of distributed LF captures), which facilitates *cheap* and *convenient* capture of target scenes, especially the more dynamic ones.
- We have proposed a novel scale-consistent frustum volume rescaling algorithm which enables fusion of *distributed, heterogeneous* geometry embedding to be globally consistent.
- We have proposed novel learning-based processing modules, i.e., attention-guided multi-scale residual fusion and deep re-regularization over the disparity field-guided LF rendering, which comprehensively regularize noisy observations from *heterogeneous* captures, and fuse these complementary features for high-quality rendering of both disparity maps and novel Light Field Images (LFIs).
- To the best of our knowledge, we have proposed the first reconstruction mechanism that can globally render a novel LF with large angular ranges and flexible optical properties (e.g., focal, exposure, and resolution settings, etc., which are determined by the target RGB image). Such a fully flexible scheme can be extended to a wide range of multi-modality sensor fusion scenarios.

The paper is organized as follows: Sec. II introduces related works and generalizes the advantages and limitations of existing IBR representation schemes. Sec. III-A describes the SCVR algorithm. Sec. III-C introduces the Frustum Voxel Filtering and Attention-Guided Multi-scale Residual Fusion Module. Sec. III-D explains the details for the disparity field synthesis and LF rendering. Section IV evaluates our proposed model and compare with existing methods. Sec. V concludes the paper.

II. RELATED WORK

For IBR, one of the most critical assumptions is accurate depth estimation. In this section, we will first review related works on depth inference based on different imaging modalities and sampling conditions. Then, different geometry embedding representations and novel view rendering methods will be reviewed and analyzed.

A. Scene Depth Inference

Depth from Multi-View Stereo (MVS). The problem of reconstructing the geometry from multi-view images is known as Structure from Motion (SfM) [18], which starts with local feature extraction, matching, geometric verification, followed by image registration, triangulation and bundle adjustment -

which filters out outliers for a refined depth reconstruction. Newcombe et al. [19] proposed a real-time camera tracking and scene reconstruction system by minimizing a global regularized energy function in a non-convex optimization framework. Pizzoli et al. [20] estimated the depths of pixels by searching for their correspondence points from multi-view images, and updates the point position by a robust probabilistic model. Schoenberger et al. [21] presented a SfM system, named as COLMAP, to reconstruct the scenes by leveraging pixel-wise photometric and geometric priors.

Conventional SfM/MVS algorithms rely on the photometric consistency assumption and show limitations in handling textureless regions and reflective surfaces. Taking advantage of the feature descriptive power of the Convolutional Neural Networks (CNN), recent works use CNNs to extract discriminative features that encode local and global information as similarity measures and have achieved significant improvements. In particular, Yao et al. [9] proposed the MVSNet which warps the reference images' feature volumes to the canonical frustum and calculates the feature matching cost which is subsequently regularized by a multi-scale 3D-UNet for the prediction of depth. Several methods have been proposed to improve the MVSNet by reducing memory cost and computational time, such as modifying the overall pipeline to a coarse-to-fine [22], sequential structure [10], adding additional edge convolution [23] or Gauss-Newton layer [24] to recover better scene geometric details. This line of methods, generalized as the entry MVSNet in TABLE I, rely on building a cost volume with continuous angular variation for efficient inference of correspondence among the depth planes, which show serious limitation dealing with sparse, large baseline reference inputs.

Depth from Light Field Images. Estimating depth from LFIs is essentially a multi-view stereo problem with denser and more regular angular sampling of the scene. Depth maps can be estimated by analyzing the slopes of lines in the epipolar-plane images (EPI) [25], [26]. In addition to EPI clues, depth can be estimated from the defocus and correspondence clues [27]. Robust regularizers such as superpixels [28] and the occlusion-aware indicators [29] can be applied to improve the boundary accuracy. In the spectrum of applying deep learning techniques for the task, Heber et al. [30] applied 3D convolutions to EPI volumes in a U-shape network architecture. Peng et al. [31] designed a combined loss function imposing both compliance and divergence constraints on the warped SAIs to the central view to predict the disparity in an unsupervised framework. Shin et al. [32] utilized a multi-stream input including SAIs organized in horizontal, vertical, left, and right diagonal directions to fully explore the angle information. Guo et al. [33] proposed to train a sub-network to explicitly predict the occlusion regions for better handling of these most challenging areas. These prediction methods, represented by the entries LBVS and FLeXLF in TABLE I, can only handle small spatial/angular baseline inputs within the camera aperture.

Depth from Monocular Image. Estimating scene depth based on a single image is challenging as it lacks reliable geometrical clues from multi-view observations. With the rise of deep learning techniques that learn and consolidate clues

TABLE I

COMPARISON OF STATE-OF-THE-ART GEOMETRY/APPEARANCE REPRESENTATION FRAMEWORKS FOR NOVEL VIEW SYNTHESIS AND IMMERSIVE RENDERING. WHILE OTHER FRAMEWORKS REQUIRE SPECIFIC OR OPTIMIZED SAMPLING PATTERNS AND SHOW VARIOUS LIMITATIONS IN RENDERING CAPABILITIES, OUR METHOD IS ROBUST TO LARGE BASELINE SPARSE INPUTS WITH DIVERSE CAMERA ANGLES.

Methods	Representation Scheme		Sampling Requirements			Rendering Capabilities	
	Embedding Repres.	Dimension of Repres.	Capture Dist. (Baseline)	Camera Angle Range	Sampling Pattern	Spatial Range	Angle Range
SynSin [13]	Feature Point Clouds	3	Single View	Single View	Single View Image	Small	Small
MPNeuPts [6]	Multi-plane Projected Neural Point Clouds	3	Large	Large	Complete Point Clouds	Large	Large
LBVS [14]	Disparity Map	2	Aperture ‡	Aperture ‡	Sparse Sub-Aperture ‡	Aperture ‡	Aperture ‡
ExtremeView [15]	Depth Plane Frustum Voxels (Prob. Vol.)	2.5 †	Very Small	Very Small	Locally Sparse	Small	Large
FlexLF [16]	Disparity Map	2	Aperture ‡	Aperture ‡	Sparse Sub-Aperture ‡	Aperture ‡	Aperture ‡
LLFF [4]	Multiple Multi-Plane Images	2.5	Px/DP §	Small (Ideally Fronto-Parallel)	Irregular Local Grid	Small	Small
MVSNet [9]	Depth Plane Frustum Voxels (Cost Vol.)	2.5 †	Small	Small (Ideally Fronto-Parallel)	Globally Dense	Small	Small
DeepVoxels [7]	Feature Voxels	3	Small	Small	Globally Dense (Hemisphere)	Large	Large
NeRF [8]	Multi-layer Perceptron Parameters	5	Small	Small	Globally Dense (Hemisphere)	Large	Large
Ours	Depth Plane Frustum Voxels (Prob. Vol.)	2.5 †	Large	Large	Globally Sparse	Large	Large

† 2.5 stands for the dimension for representations in which the z dimension is coarsely sampled (e.g., by depth planes).

‡ *Aperture* indicates that the distance and angle differences between two adjacent captures are within the camera main lens’ aperture diameter and its field-of-view angle, respectively.

§ *Px/DP* indicates maximum camera lateral movement which causes shift of *one pixel* between any adjacent depth planes [17].

such as shading, texture, and semantics, models trained over RGB-D datasets [34] demonstrate visually and perceptually satisfying depth prediction results. Ren et al. [35] proposed a zero-shot cross-dataset training strategy to leverage a variety of datasets. Nonetheless, the prediction accuracy based on monocular images cannot be guaranteed due to the scale and semantic ambiguities.

B. Scene Representation frameworks for Novel View Synthesis

As generalized in TABLE I, several seminal scene geometry/appearance representation frameworks have been developed in recent years, which are able to synthesize high-quality views from novel angles. We review these representations and analyze their respective advantages and limitations.

Multi-plane Images. The seminal multi-plane image (MPI) model [2], [4], [17] analyzes the scene geometry over plane-sweep volumes and projects pixels into a set of fronto-parallel RGB- α planes within the reference camera’s view frustum. Novel views are rendered by homography-warping and over-compositing the RGB- α planes. Based on the MPI representation, Flynn et al. [36] incorporated learned gradient descent mechanism. Srinivasan et al. [17] enforced a layer constraint for the occluded pixels. Choi et al. [15] dealt with occlusion and depth uncertainty with a depth probability volume and combined multiple warping clues over large extrapolation angles for robust fusion. Local Light Field Fusion [4] renders novel views by blending re-weighted MPIs generated from a set of input images. This method requires capture locations to be approximately on the same plane so that the discretized depth planes among views could be aligned with each other for efficient fusion. Represented by the entries LLFF and MVSNet in TABLE I, methods based on *layered homography*

transform assume a flattened fronto-parallel depth distribution with only rotating or planar-moving camera motions, which limit its performance in synthesizing complex scenes over flexible camera shooting angles. In addition, the maximum camera lateral movement is limited by its causal shift between any adjacent depth plane by one pixel [17].

Neural Implicit Functions. As an alternative to conventional IBR methods, neural rendering methods avoid explicit warping operations and directly encode the scene into the parameters of an Multi-layer Perception (MLP) network which can map spatial 3D query points into RGB- α values [8], signed distance values [37], [38] or occupancy field values [39]. Sitzmann et al. [7] proposed to learn a DeepVoxels representation from 2D images without explicitly modeling the scene geometry. Mildenhall et al. [8] proposed to represent the scene as a continuous volumetric function which directly maps a 5D coordinate (for the observation ray) to output colors and densities. As represented by the entries DeepVoxels and NeRF in TABLE I, these models require dense sampling (more than 100 captures) of a compact target area and are not scalable for larger scenes.

Point-based Representations. Using points as rendering primitives has been an active research topic recently [40]. Point clouds bear explicit geometric properties which make them flexible to rotate to an arbitrary viewpoint for rendering. Points can be encoded as latent appearance vectors and rendered by a deep frame buffer for realistic effects [41]. Wiles et al. [13] used spatial feature network to extract higher-level representation from input RGB colors. Feature point clouds are then transformed and rendered by the neural point cloud renderer, which softens the hard z-buffer via using alpha over-compositing. The unstructured nature of point clouds has driven most researchers to transform them to regular 3D

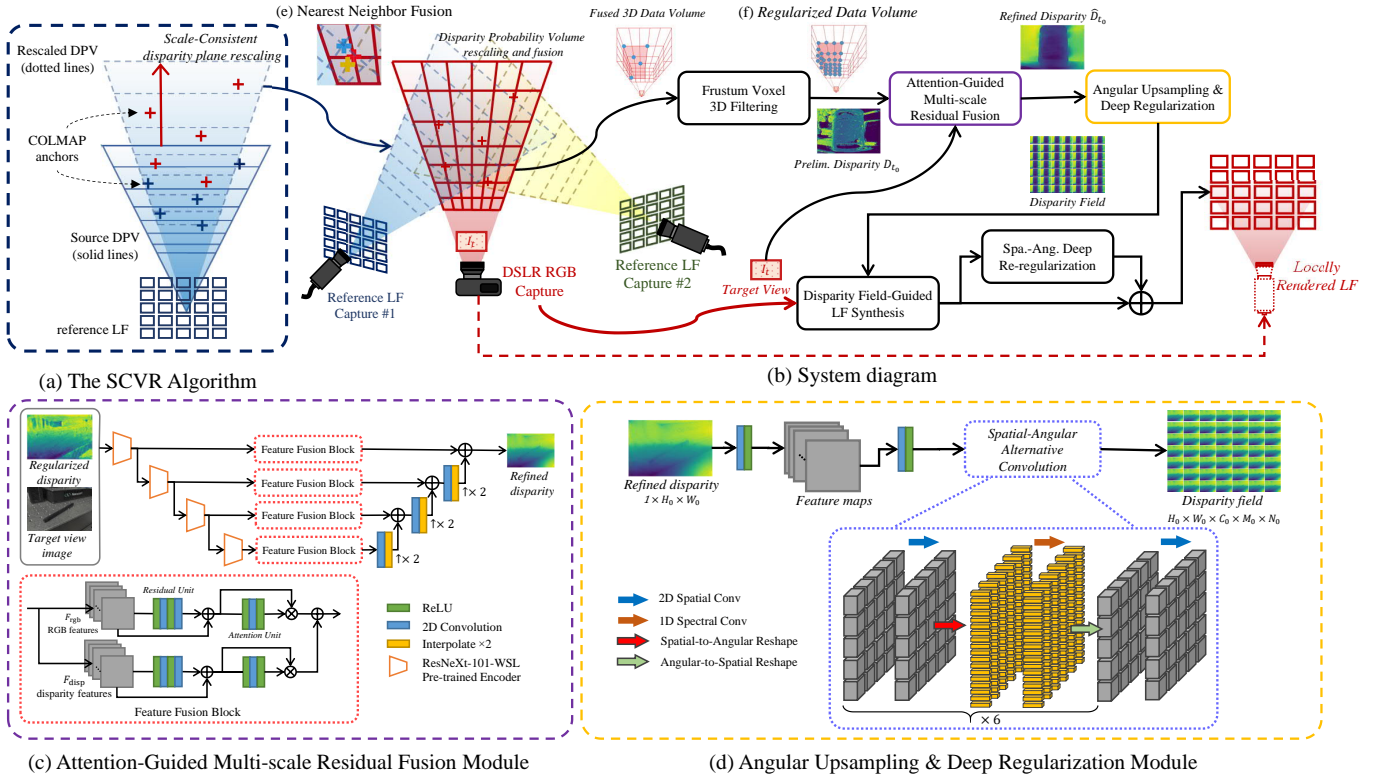


Fig. 1. The overall pipeline of our proposed method. 1) The source *heterogeneous* LFs’ DPVs are rescaled to be scale-consistent by our Scale-Consistent Volume Rescaling algorithm, then the disparity planes of the DPVs are aligned for accurate warping and blending. 2) A Frustum Voxel Filtering Module is proposed to complete the DPVs. 3) The Attention-Guided Multi-scale Residual Fusion Module performs RGB-D fusion to produce a high-quality disparity map. 4) The LF is finally synthesized by backward warping pixels of target view image with estimated accurate disparity prior and further refined by spatial-angular convolutional blocks.

voxel grids. For example, multi-plane based voxelization and multi-plane rendering are adopted in [6]. As represented by the entry *SynSin* and *MPNeuPts* in TABLE I, rendering the unstructured point clouds requires computationally expensive pre-processing (e.g., voxelization) and z-buffering operations.

Local Immersive Light Field Synthesis. LFI itself is also a powerful scene representation with scene geometry and view-dependent effects embedded within its 4D spatial-angular structures. Researchers have focused on synthesizing complete LFIs from sparse inputs. Early algorithms rely on the plenoptic function and take LF synthesis as a re-sampling task [42]. Without accurate geometry estimations, this approach can only synthesize novel views with small baselines. Some works attempt to synthesize LFIs with geometric [43]. Some enforce priors over the Fourier spectrum [44] and the Shearlet transform domain [45]. Kalantari et al. [14] made the first attempt to use CNNs to synthesize novel LFIs from a sparse set of inputs, with a system that can be broken down into disparity and color estimation modules. Srinivasan et al. [46] used two convolutional neural networks to synthesize a 4D RGB-D LF from a 2D RGB image, where the first CNN estimates the scene geometry and the second predicts occluded rays and non-Lambertian effects. Yeung et al. [47] introduced a fast LF reconstruction from a sparsely-sampled LF in a coarse-to-fine manner and explored the dense spatial and angular clues by spatial-angular alternative convolutions. Wu et al. [48] restored the angular detail by using Deep Convolutional Network on

EPI.

III. PROPOSED METHOD

Given N_{src} sets of source LFIs $\{\mathbf{L}_t \in \mathbb{R}^{H_t \times W_t \times M_t \times N_t}\}_{t=1}^{N_{\text{src}}}$ which capture the scene from *large diverse* viewing positions, our model $\mathcal{F}(\cdot)$ aims to accurately fuse these source information and synthesize a novel immersive LF $\hat{\mathbf{L}}_{t_0} \in \mathbb{R}^{H_0 \times W_0 \times C_0 \times M_0 \times N_0}$ which is aligned to an image capture $I_{t_0} \in \mathbb{R}^{H_0 \times W_0 \times C_0}$ at a target angle t_0 :

$$\hat{\mathbf{L}}_{t_0} = \mathcal{F}(\{\mathbf{L}_t\}_{t=1}^{N_{\text{src}}}, I_{t_0}; \theta), \quad (1)$$

here H_t, W_t indicate the spatial dimensions of the source LFIs, M_t, N_t indicate the angular dimensions of the source LFIs, respectively. H_0, W_0, C_0 indicate the spatial and channel dimensions of the target RGB capture, and M_0, N_0 indicate the angular dimensions of the synthesized immersive LFI $\hat{\mathbf{L}}_{t_0}$. θ stand for the parameters of the learning modules.

The overall pipeline of our proposed framework is illustrated in Fig. 1, which consists of five steps. *First*, a Disparity Probability Volume¹ (DPV) $\{\mathbf{V}_t \in \mathbb{R}^{W_t \times H_t \times N_{\text{dp}}}\}_{t=1}^{N_{\text{src}}}$ is estimated for each of the source LFI. Here N_{dp} stands for the number of disparity/depth planes. To ensure all the DPVs are scale-consistent, we rely on COLMAP [21], [49], a well adopted structure-from-motion pipeline, to estimate the source

¹DPV is calculated with the slope of EPI line which is proportional to the disparity value [28], the confidence of the slope estimation represents the probability of its corresponding disparity value.

view camera poses and establish a set of 3D points as reliable 3D anchors among the source LFIs. The Scale-Consistent Volume Rescaling (SCVR) algorithm is proposed to realign the DPVs based on these reliable 3D anchors, which produces a set of scale-consistent DPVs $\{\mathbf{U}_t\}_{t=1}^{N_{\text{src}}}$. *Second*, the disparity probability values within the source rescaled DPVs $\{\mathbf{U}_t\}_{t=1}^{N_{\text{src}}}$ are *homography warped* to the fronto-parallel planes of the target camera’s frustum, and fused as a 3D data volume \mathbf{U}_{t_0} . *Third*, to comprehensively exploit the geometrical information in \mathbf{U}_{t_0} , the Frustum Voxel Filtering Module is deployed to explore the information in \mathbf{U}_{t_0} for a coarse disparity estimation $D_{t_0} \in \mathbb{R}^{H_0 \times W_0}$. *Fourth*, the Attention-Guided Multi-scale Residual Fusion Module is designed to refine D_{t_0} with the textural and semantic guides from the target view image I_{t_0} in a multi-scale, progressive manner, and produce the final disparity estimation \hat{D}_{t_0} . *Finally*, a Disparity Field-Guided Deep Re-regularization Module is proposed to raise I_{t_0} into a locally immersive LF $\hat{\mathbf{I}}_{t_0}$ by back-warping and deep spatial-angular regularization. In the following subsections, we will elaborate the details for each sub-module.

A. The Scale-Consistent Volume Rescaling Algorithm

Depth estimation based on a single LF is essentially a multi-view stereo problem with the virtual cameras of SAIs *densely and regularly* positioned, enabling efficient algorithms to be developed for high precision sub-pixel level parallax estimation. A DPV $\mathbf{V}_t(x, y, d) \in \mathbb{R}^{H_t \times W_t \times N_{\text{dp}}}$ can be estimated, which reflects each pixel’s probability distribution with respect to each disparity plane. Based on the DPV $\mathbf{V}_t(x, y, d)$, an initial disparity map D_{init} can be calculated [27], [28].

The exact *object space distance* that each DPV’s *disparity interval* corresponds to varies between different captures, which is decided by the capture settings (e.g., focal length settings). Therefore, before $\{\mathbf{V}_t\}_{t=1}^{N_{\text{src}}}$ can be coherently fused together to the target camera’s viewing frustum, a *rescaling* process must be implemented to ensure the scale-consistency of the DPVs among the source views. To this end, we propose a Scale-Consistent Volume Rescaling algorithm which iteratively performs rescaling, trimming and interpolation operations over the DPVs.

We first use COLMAP [21] to analyze the scene geometry based on the central views of the source LFIs $\{I_t\}_{t=1}^{N_{\text{src}}}$ and the 2D image I_{t_0} from the target viewing angle. COLMAP outputs the camera parameters for each view, along with a set of *sparse but reliable* 3D points $\mathcal{P}(x, y, z)$ which establish correspondences among the 2D pixels from $I_{t_0} \cup \{I_t\}_{t=1}^{N_{\text{src}}}$. With slight abuse of notation, we use $\mathcal{P}_t(x, y)$ to represent the 2D image coordinates in $\{I_t\}_{t=1}^{N_{\text{src}}}$ which are projected from the 3D points $\mathcal{P}(x, y, z)$ in *world coordinate*, and use $\mathcal{P}_t(z)$ to represent the depth of $\mathcal{P}(x, y, z)$ with respect to the image plane of view t . The 3D point $\mathcal{P}(x, y, z)$ is visible to multiple views, the depth $\mathcal{P}_t(z)$ is a cross-view consistent value in *world coordinate*.

We want to rescale the DPVs to be cross-view consistent via minimizing the difference between depth $\mathcal{P}_t(z)$ and its corresponding disparity value in D_{init} . Therefore, we transform the initial disparity estimation $D_{\text{init}}(\mathcal{P}_t(x, y))$ to depth values

Algorithm 1: The Scale-Consistent Volume Rescaling algorithm (SCVR).

- **Input:** Sparse 3D anchors \mathcal{P} ; DPV \mathbf{V}_t ; COLMAP depth range κ ; Iterative times N ; Initial disparity map D_{init} .
- **Output:** rescaled DPV $\bar{\mathbf{U}}_t$.
- **Algorithm:**
- Initialize $\{\alpha, \beta\}$ as Eq. (3) with D_{init} and \mathcal{P} ;
while $n \leq N$ **do**
 Update the $\Psi_{\alpha, \beta}$ and $\{\alpha, \beta\}$ as Eq. (2, 3);
 Update the \mathbf{V}_t with $\Psi_{\alpha, \beta}$ to produce \mathbf{U}_t as Eq. (4);
 Discard planes exceeding κ from \mathbf{U}_t to produce \mathbf{U}_t^γ as Eq. (5);
 Interpolate the \mathbf{U}_t^γ to $\bar{\mathbf{U}}_t$ as Eq. (6);
 $n = n + 1$;
end

via:

$$\Psi_{\alpha, \beta}(D_{\text{init}}(\mathcal{P}_t(x, y))) = \frac{\alpha}{D_{\text{init}}(\mathcal{P}_t(x, y))} + \beta. \quad (2)$$

Here $\Psi_{\alpha, \beta}$ is a mapping function that reflects the inverse-proportional relationship between the absolute depth and the capture-specific disparity. α is related to the focal length and the camera baseline; β is the bias parameter. $\{\alpha, \beta\}$ can be determined by minimizing the alignment error given by

$$\{\alpha, \beta\} = \arg \min_{\alpha, \beta} \|\Psi_{\alpha, \beta}(D_{\text{init}}(\mathcal{P}_t(x, y))) - \mathcal{P}_t(z)\|_2^2. \quad (3)$$

The estimated parameters $\{\alpha, \beta\}$ can subsequently be used to transform all disparity planes in \mathbf{V}_t to produce \mathbf{U}_t :

$$\mathbf{U}_t = \Psi_{\alpha, \beta}(\mathbf{V}_t). \quad (4)$$

After each transformation iteration, depth planes in \mathbf{U}_t that exceeds COLMAP’s depth range κ will be trimmed and discarded:

$$\mathbf{U}_t^\gamma = \Gamma_{\text{trim}}(\mathbf{U}_t) : \mathbb{R}^{H \times W \times N_{\text{dp}}} \mapsto \mathbb{R}^{H \times W \times N'_{\text{dp}}}, \quad (5)$$

where N'_{dp} is the remaining number of planes in \mathbf{U}_t^γ after trimming. This is subsequently followed by a linear interpolation process along the depth dimensions N'_{dp} to produce a new probability volume $\bar{\mathbf{U}}_t$ which preserves its original disparity plane resolution N_{dp} :

$$\bar{\mathbf{U}}_t = \Gamma_{\text{interp}}(\mathbf{U}_t^\gamma) : \mathbb{R}^{H \times W \times N'_{\text{dp}}} \mapsto \mathbb{R}^{H \times W \times N_{\text{dp}}}. \quad (6)$$

Note that the procedures defined from Eq. (2) to Eq. (6) will be repeated for N times until convergence. In our experiments, $N=7$ generally gives satisfactory results. This iteration process helps to progressively remove redundant planes. Each iteration generates a more *compact* volume with higher disparity resolution, ensuring higher alignment accuracy than the one-off rescaling.

In summary, the operator $\Psi_{\alpha, \beta}$ *stretches* or *compresses* the DPVs to be scale-consistent among all source views; Γ_{trim} selects the depth cut-off range; and Γ_{interp} interpolates the DPVs to a consistent resolution. The pseudo code of the SCVR algorithm has been generalized in Algorithm 1.

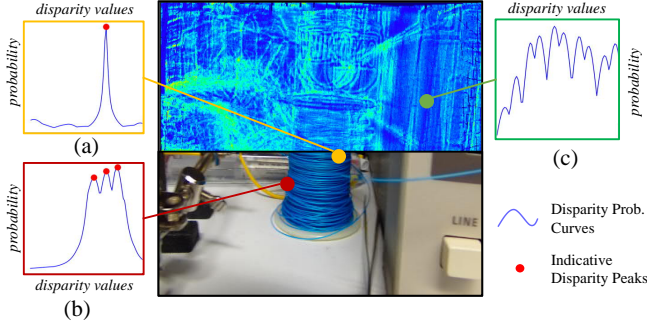


Fig. 2. Disparity probability distribution along a light ray.

Remark. The SCVR algorithm is based on reliable COLMAP spatial anchors. These anchors are crucial for consistent fusion of *heterogeneous* source volumes, and for flexible projection with accurate alignment to target RGB capture’s optical properties.

B. Probability Volume Fusion

The values in the rescaled probability volume $\bar{\mathbf{U}}_t$ indicate the pixels’ probability of having correct disparity at the corresponding plane, *based on the observation from \mathbf{L}_t* . As visualized in Fig. 2(a), a peak along the disparity axis can be observed for regions with clear textures, which gives strong indication on its correct disparity value. However, for textureless regions (Fig. 2(b)) or near regions with depth discontinuities (Fig. 2(c)), the probability distributions provide less informative indications. Nevertheless, when these weak and implicit clues are fused from multiple observation angles and interpreted in a *spatially* and *semantically* congruent manner, we expect a much more confident prediction. This motivates us to investigate a robust fusion mechanism for accurate target view geometry inference.

We apply *Homography Warping* $\mathcal{H}(d)$ to transform the source volumes $\{\bar{\mathbf{U}}_t\}_{t=1}^{N_{\text{src}}}$ to the target camera’s frustum. The coordinates mapped from the source viewpoint t to the target viewpoint t_0 is determined by the planar homography transformation:

$$\mathbf{U}_{t \rightarrow t_0}(x, y, d) = \mathcal{H}(d) \cdot \bar{\mathbf{U}}_t(x, y, d). \quad (7)$$

The homography warping operator $\mathcal{H}(d)$ is defined as:

$$\mathcal{H}(d) = K_t \cdot R_t \cdot \left(\mathbf{I} - \frac{(\tau_t - \tau_{t_0}) \cdot n_{t_0}^T}{d} \right) \cdot R_{t_0}^T \cdot K_{t_0}^T, \quad (8)$$

where $n_{t_0}^T$ denotes the principle axis of the target camera frustum, and $\{K, R, \tau\}$, estimated by COLMAP, denote the camera *intrinsics*, *rotation* and *translation* matrices, respectively. As demonstrated in Fig. 1, after the homography warping, all the disparity planes from the volumes $\bar{\mathbf{U}}_t$ are transformed as fronto-parallel planes onto the target view camera’s frustum.

To efficiently fuse the source camera’s probabilities to the target camera’s probability volume, $\mathbf{U}_{t_0}(x, y, d)$ is estimated by fusing the nearest probability bins (as shown in Fig. 1(e))

from $\mathbf{U}_{t \rightarrow t_0}$ via:

$$\mathbf{U}_{t_0}(x, y, d) = \frac{\sum_t W_t^{\text{pos}} \cdot W_t^{\text{dir}} \cdot \mathbf{U}_{t \rightarrow t_0}(x, y, d)}{N_{\text{rays}}}. \quad (9)$$

Here N_{rays} stands for the count of *contributing sources* at the current bin. W_t^{pos} and W_t^{dir} are fusion weights that take source camera’s location and frustum direction differences into account during fusion: source cameras with larger position and directional differences to the target camera are less reliable and should contribute less during fusion. Both W_t^{pos} and W_t^{dir} are normalized by the softmax function with euclidean distances from all source cameras. Fig. 3 gives visual demonstrations of the fused 3D data volume \mathbf{U}_{t_0} .

Remark. Compared with MVSNet [9], or the other multi-view stereo methods that also perform homography warping on images or features, we directly work on probability distributions. Our method has two advantages: first, the generation of source view features requires larger memory and intensive computation, which usually require down-sampling of feature resolutions and thus limit the quality of estimated geometry; second, fusion of probability distribution is much more robust compared to direct fusion of image features. It combines weak probability clues into stronger ones via the weighted fusion mechanism as in Eq. (9). This enables our framework to deal with larger baseline scenarios.

C. Frustum Voxel Filtering and Attention-Guided Multi-scale Residual Fusion.

The fused 3D data volume $\mathbf{U}_{t_0}(x, y, d) \in \mathbb{R}^{H_0 \times W_0 \times N_{\text{dp}}}$ sub-divides the camera’s visible space into frustum voxels (FV). As can be observed from Fig. 3, there are explicit peaks and less *smearing effect*² over regions with edges and textures. However, a significant amount of FVs are noisy and without explicit values over texture-less regions. In order to propagate correct probability values to the relevant FVs, we utilize a 3D-UNet structure (network detail specified in TABLE II) to further filter the frustum data. The output will be a deeply regularized volume $\hat{\mathbf{U}}_{t_0}$ as shown in Fig. 1(f), over which, a preliminary disparity map D_{t_0} will be generated as weighted sum over all hypothesized planes:

$$D_{t_0}(x, y) = \sum_d \hat{\mathbf{U}}_{t_0}(x, y, d) \times d. \quad (10)$$

To further improve the quality of D_{t_0} by ensuring boundary alignment and semantic consistency with the target view RGB capture I_{t_0} , an Attention-Guided Multi-scale Residual Fusion Module is designed which progressively combines encoded features from the target image $F_{t_0}^i$ with the features from the preliminary disparity map F_{disp}^i in a multi-scale and coarse-to-fine manner. The structure of the module is shown in Fig. 1(c). *ResNeXt-101-WSL* [35], [50] has been adopted as feature encoder. As specified from Eq. (11) to (16), the final refined disparity map \hat{D}_{t_0} at the target view is generated by fusing multi-scale residuals $R_{t_0}^i, R_{\text{disp}}^i$ (upsampled by Γ_{up}) weighted

²Each FV stores the disparity probability value that is homography warped and fused from multi-LF observations. The smearing effect is caused by the dispersion of probability peaks during warping.

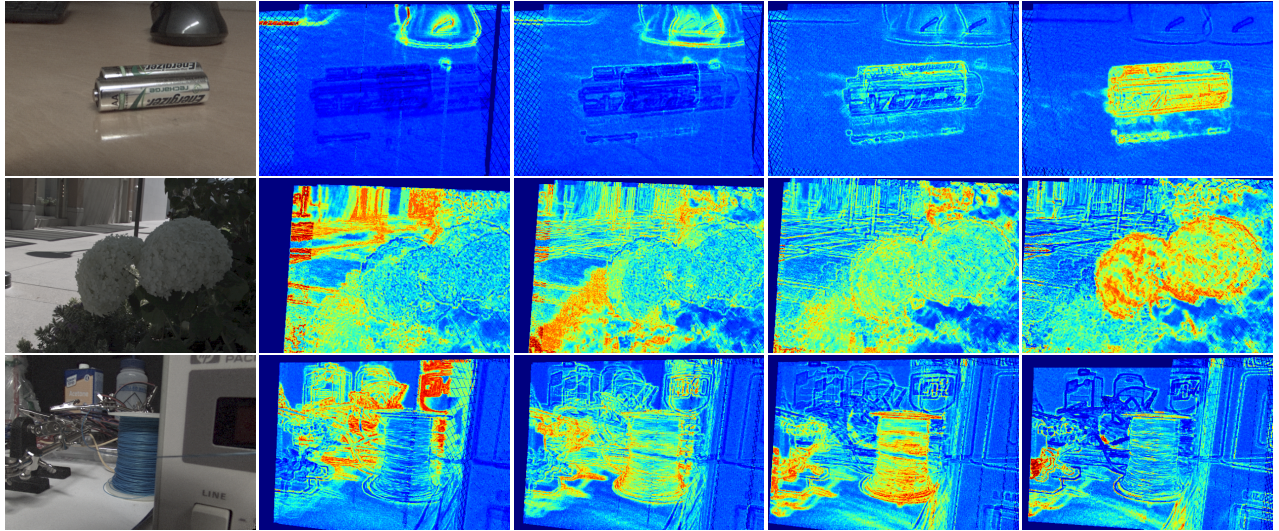


Fig. 3. Illustration of DPV fusion outcomes. Images on the leftmost column are the target view image I_{t_0} . Images starting from the second column to the right show the disparity probability values from disparity planes $d = 20$ to 80 (100 planes in total). Brighter pixels indicate higher probability.

TABLE II

NETWORK STRUCTURE OF THE FRUSTUM Voxel FILTERING MODULE. HERE k DENOTES 3D KERNEL SIZE (AS $k \times k \times k$), s DENOTES STRIDE, d DENOTES NUMBER OF PADDING, C_{IN} DENOTES THE NUMBER OF INPUT FEATURE CHANNEL, C_{OUT} DENOTES THE NUMBER OF OUTPUT FEATURE CHANNEL.

Layer	k	s	d	C_{in}	C_{out}	Input	Output
Conv 0_1	3	1	1	1	10	\mathbf{U}_{t_0}	$V_{0,1}$
Conv 1_0	3	2	2	10	20	$V_{0,1}$	$V_{1,0}$
Conv 2_0	3	2	2	20	40	$V_{1,0}$	$V_{2,0}$
Conv 3_0	3	2	1	40	120	$V_{2,0}$	$V_{3,0}$
Conv 1_1	3	1	1	20	20	$V_{1,0}$	$V_{1,1}$
Conv 2_1	3	1	1	40	40	$V_{2,0}$	$V_{2,1}$
Conv 3_1	3	1	1	120	120	$V_{3,0}$	$V_{3,1}$
Conv 3_2	3	2	1	120	40	$V_{3,1}$	$V_{3,2}$
Conv 2_2	3	2	2	40	20	$V_{2,1} + V_{3,2}$	$V_{2,2}$
Conv 1_2	3	2	2	20	10	$V_{2,2} + V_{1,1}$	$V_{1,2}$
Conv 0_2	1	3	1	10	1	$V_{0,1} + V_{1,2}$	$\hat{\mathbf{U}}_{t_0}$

based on the predicted attention masks $W_{t_0}^i$ and W_{disp}^i , which help to locate informative regions for efficient residual fusion.

$$R_{disp}^i = \text{conv}(\text{ReLU}(\text{conv}(\text{ReLU}(F_{disp}^i)))) + F_{disp}^i, \quad (11)$$

$$R_{rgb}^i = \text{conv}(\text{ReLU}(\text{conv}(\text{ReLU}(F_{rgb}^i)))) + F_{rgb}^i, \quad (12)$$

$$W_{disp}^i = \text{ReLU}(\text{conv}(\text{ReLU}(R_{disp}^i))), \quad (13)$$

$$W_{rgb}^i = \text{ReLU}(\text{conv}(\text{ReLU}(R_{rgb}^i))), \quad (14)$$

$$\Gamma_{up}[\cdot] = \text{Interpolate}(\text{conv}(\cdot)), \quad (15)$$

$$\hat{D}_{t_0}^i = W_{disp}^i \odot R_{disp}^i + W_{rgb}^i \odot R_{rgb}^i + \Gamma_{up}[\hat{D}_{t_0}^{i-1}], \quad (16)$$

where i is the scale index of the decoder. The operator Γ_{up} upsamples the feature by 2 using a bilinear interpolator.

D. Disparity Field Synthesis and Immersive Rendering

The final step of our framework is to utilize the refined disparity map to raise the target view image $I_{t_0} \in \mathbb{R}^{H_0 \times W_0 \times C_0}$ into a locally immersive LF: $\hat{\mathbf{L}}_{t_0} \in \mathbb{R}^{H_0 \times W_0 \times C_0 \times M_0 \times N_0}$. This

involves two sub-steps: disparity field synthesis and immersive content rendering.

Disparity Field Synthesis. The goal of this module is to raise the disparity map $\hat{D}_{t_0} \in \mathbb{R}^{H_0 \times W_0}$ into a densely-sampled immersive field $\mathbf{F} \in \mathbb{R}^{H_0 \times W_0 \times M_0 \times N_0}$. Each angular slice of \mathbf{F} represents the parallax of the sub-aperture view with respect to I_{t_0} . As shown in Fig. 1(d), the disparity field synthesis network takes $\hat{D}_{t_0} \in \mathbb{R}^{H_0 \times W_0 \times 1}$ as input, and first uses a 2D convolution layer to upsample the channel dimension of \hat{D}_{t_0} from 1 to $M_0 \times N_0$. The convolution layer learns the spatial-angular parallax correlations among the upsampled angular channel slices, and they are further regularized by a Spatial-Angular Alternating (SAA) Convolution Module [47], [51], [52], which finally generates the spatial-angular consistent disparity field. The SAA Convolution Module consists of a set of Spatial-Angular Convolution Blocks; each block performs pseudo-4D convolutions by alternatively carrying out 2D convolutions on the spatial and angular dimensions of the 4D data. The SAA module deeply regularizes the implicit structures of the disparity field in a computationally efficient manner.

Immersive Content Rendering. Compared with previous methods of synthesizing LF using a sparse set of input views [14], [46], synthesizing an immersive LF from a single image is much more challenging. Nonetheless, we can fully exploit the accurate scene geometric prior \mathbf{F} to backward warp pixels from the target view I_{t_0} to other SAIs as illustrated in Eq. (17).

$$\mathbf{L}_{t_0}(\mathbf{x}, \mathbf{v}) = I_{t_0}(\mathbf{x} + \mathbf{F}(\mathbf{x}, \mathbf{v}) \times \mathbf{v}), \quad (17)$$

where \mathbf{x} is the 2D coordinates in I_{t_0} , $\mathbf{v} \in [0, M_0 \times N_0]$ is the angular index of the SAI, \mathbf{v} is the angular offsets between the \mathbf{v} -th SAI with respect to the central view, \mathbf{L}_{t_0} is the synthesized preliminary LF. The preliminary LF is further refined by adding the residual from a second SAA module with the same network structure as the one in the disparity field network. Consequently, the output of the Immersive Content Rendering is a refined LF $\hat{\mathbf{L}}_{t_0}$.

Remark. We have employed the methodology of first synthesizing the disparity field and based on which, subsequently synthesizing the light field. SAA module has been applied twice, which efficiently *re-regularizes* the structure of the high dimensional LF data. The high-quality disparity estimation \hat{D}_{t_0} is also the main reason for high-quality LF synthesis.

E. Model Implementation Details

The Loss Function: The training of the FV Filtering Module and the Attention-Guided Multi-scale Residual Fusion Module are supervised by \mathcal{L}_{fv} and \mathcal{L}_{fused} , both of which are calculated as the sum of multi-scale Mean Square Error (MSE) between D_{t_0} and \hat{D}_{t_0} with respect to the ground truth disparity D_g , as shown in Eq. (18) and (19). The final loss for disparity estimation \mathcal{L}_{final} is the sum of \mathcal{L}_{fv} and \mathcal{L}_{fused} as shown in Eq. (20).

$$\mathcal{L}_{fv}(D_{t_0}, D_g) = \sum_{i=1}^{N_{scale}} \text{MSE}(D_{t_0}^i, D_g^i), \quad (18)$$

$$\mathcal{L}_{fused}(\hat{D}_{t_0}, D_g) = \sum_{i=1}^{N_{scale}} \text{MSE}(\hat{D}_{t_0}^i, D_g^i), \quad (19)$$

$$\mathcal{L}_{final} = \mathcal{L}_{fv}(D_{t_0}, D_g) + \lambda_{fv} \mathcal{L}_{fused}(\hat{D}_{t_0}, D_g). \quad (20)$$

Here i is the scale index for the residual feature fusion module (with N_{scale} scales in total); D_g is the ground truth disparity; and λ_{fv} is the balance weight for the loss \mathcal{L}_{fused} .

The Light Field Synthesis Module is supervised by the composite loss \mathcal{L}_{lf} of MSE, Mean Absolute Error (MAE) and the epipolar-plane image (EPI) losses between the synthesized LF $\hat{\mathbf{L}}_{t_0}$ and the ground truth LF \mathbf{L}_{gt} :

$$\mathcal{L}_{lf} = \text{MSE}(\mathbf{L}_{gt}, \hat{\mathbf{L}}_{t_0}) + \lambda_1 \text{MAE}(\mathbf{L}_{gt}, \hat{\mathbf{L}}_{t_0}) + \lambda_2 \text{EPI}(\mathbf{L}_{gt}, \hat{\mathbf{L}}_{t_0}). \quad (21)$$

Here λ_1, λ_2 are the balance weights for respective losses.

The Dataset Details: For model training and evaluation, we used the *Stanford Lytro Multi-view Light Field Dataset* (MVLf) [53], which contains a set of scenes organized as 30 categories. Each category contains LFIs captured over the same target scene from 3 to 5 camera poses. We have selected 127 scenes³, of which 109 are used for training and 18 for evaluation. We used COLMAP to estimate the camera parameters K, R, τ and the sparse 3D point anchors \mathcal{P} based on the central views of each LF. Since there are no ground truth disparity maps directly provided by the MVLf dataset, we generated the disparity maps using the state-of-the-art LF depth estimation method [28] as the ground truth.

Training and Implementation Details. The proposed framework has been implemented with PyTorch 1.7.1. The disparity estimation model and the LF synthesis model were trained in two stages.

For the *Disparity Estimation Model*, the *Adadelta* optimizer [54] was used for training, with batch-size set to four. The learning rate was initialized to 0.01, with decay rate 0.9

starting from the tenth epoch. Each training sample consists of one target view’s color image I_{t_0} , ground truth disparity map D_g , and the pre-computed fused 3D data volume $\mathbf{U}_{t_0} \in \mathbb{R}^{376 \times 541 \times 100}$. The feature scale number N_{scale} for the multi-scale fusion module was set to seven, and the number of disparity planes was set to 100. To improve training efficiency, we have pre-calculated the target view’s fused 3D data volumes $\mathbf{U}_{t_0}(x, y, d)$ off-line and used them directly during training.

For the training of the *The LF Synthesis Model*, the *Adadelta* optimizer [54] was used with batch size set to one. The learning rate was initialized to 0.00001, with decay rate 0.5 starting from the second epoch. The angular resolution of the ground truth LF in the MVLf dataset is 14×14 , and we only render the central 7×7 SAIs to avoid vignetting effects. The LF synthesis model took 24 hours to train from scratch for 120 epochs on an NVIDIA Tesla V100S GPU.

IV. EVALUATION AND RESULTS

In this section, we will comprehensively evaluate the efficiency of the proposed disparity estimation and the immersive LF rendering modules. We will also compare our method with several state-of-the-art novel view/LF synthesis frameworks to validate the advantages of the proposed method.

A. Evaluation on Disparity Prediction

We evaluate the disparity estimation accuracy and compare the results of our proposed method with the state-of-the-art methods, i.e., MiDaS [35], Multi-View Stereo Network (MVSNet) [9], and Local Light Field Fusion (LLFF) [4], based on different input configurations. Both MVSNet and LLFF can predict the target view’s depth map given several source views as reference, while MiDaS works on a single image to predict the scene depth.

For fair comparison, we intended to use all SAIs ($7 \times 7 = 49$ SAIs for each LF) available from the source LFs as input for the MVSNet. Due to the memory limit, only 11 views are allowed to be used as input. To obtain the best results from MVSNet and LLFF, we experimented on using different input configurations, denoted as *CVs*, *FCVs*, and *FSAIs*, respectively. As illustrated in Fig. 5(a), for *CVs*, the target view image, together with the central SAIs from its two neighboring source LFs are used as inputs; therefore, three images are used as inputs in total for this configuration. For *FCVs* (illustrated in Fig. 5(b)), central SAIs from all LFs (4 to 6) under the same MVLf scene and the target view image are used as inputs for geometry inference. For *FSAIs* (illustrated in Fig. 5(c)), the target view image, together with the central, and the four corner SAIs from its two neighboring source LFs are used as inputs; therefore, totally 11 images are used as inputs in this case. For *CV*, only the target view image is used.

The depth estimation results from MiDaS, MVSNet, and LLFF, are in different scales compared with the ground truth disparity D_g . So these estimations are *linearly rescaled* (including inverse operations that transforms depth to disparity values) to be aligned with the ground truth D_g .

³Note that we have discarded several scenes from the original MVLf dataset, over which COLMAP failed to establish correspondence.

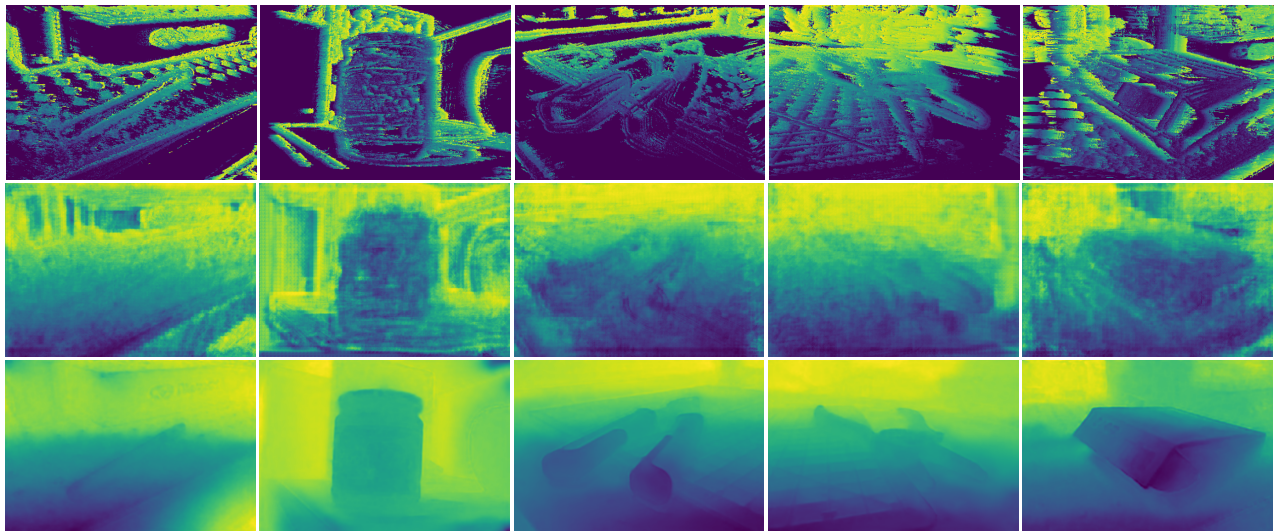


Fig. 4. The images on the first row are disparity maps directly inferred from $\bar{\mathbf{U}}_t$ before being processed by the Frustum Voxel Filtering Module. We can observe lots of blank space (in dark blue) without disparity values in the first row. The images on the second row are the preliminary disparity maps D_{t_0} inferred from the regularized DPV $\hat{\mathbf{U}}_{t_0}$, which are much better in completeness. The images on the third row are the final disparity estimations \hat{D}_{t_0} which combines texture and semantic constraints from the target view image I_{t_0} .

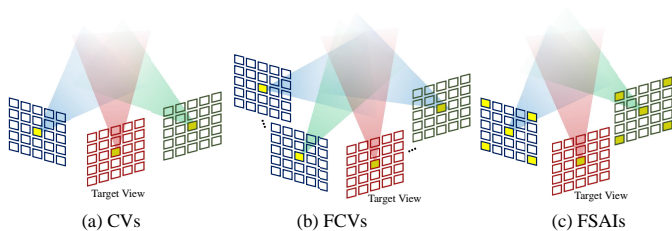


Fig. 5. Experimental set-ups for different testing cases with different SAIs from source LFIs used as source images. The selected SAIs are marked in yellow for each case.

Two metrics are used to evaluate the disparity estimation quality: MSE between the prediction and the ground truth disparity, and the Percentage of Pixels with disparity estimation Errors (PPE) smaller than a given threshold (i.e., 0.05 and 0.1). TABLE III shows the MSE and PPE results for the whole evaluation dataset, and TABLE VI shows the evaluation detail for each scene category. As can be seen from these results, our proposed algorithm significantly outperforms all other methods by almost **10 times** in the metric of MSE, and **4 times** in the metric of PPE. We believe this is caused by two reasons. *First, local structural information from the SAIs within the same LFI (for the FSAIs scenario) cannot be efficiently exploited in a global capture framework.* When these locally dense SAIs are projected to the target camera’s frustum, they are fused with features warped from large-baseline views. MVSNet treats all views equally and calculates feature variances to build cost volumes, which is overpowered by large baseline inputs. *Second, SAIs from different LFIs have very large camera pose differences, which is too challenging for these methods to extract reliable cross-view information.* However, our framework can fully take advantage of such local-global sampling patterns and produce impressive results.

We visually compare the estimated disparity maps between different methods in Fig. 6. The estimation from LLFF is

TABLE III
COMPARISON OF DISPARITY ESTIMATION ERROR MEASURED IN MSE AND PPE BETWEEN OUR PROPOSED METHOD AND MiDaS [35], LLFF [4] AND MVSNET [9]. BEST PERFORMANCE IS HIGHLIGHTED IN RED, SECOND BEST PERFORMANCE IN BLUE.

Method/Metric	MSE(px)↓	PPE(0.05,%)↑	PPE(0.1,%)↑
MiDaS (CV)	0.444	5.664	11.850
LLFF (CVs)	0.394	4.777	9.678
LLFF (FCVs)	0.354	5.248	10.557
LLFF (FSAIs)	0.447	4.772	9.789
MVSNet (CVs)	0.399	6.050	12.139
MVSNet (FCVs)	0.464	5.721	11.471
MVSNet (FSAIs)	0.449	5.761	11.297
Ours	0.050	22.878	41.740

shown in Fig. 6(c). Since the LLFF framework presumes the input source views are captured from the same fronto-parallel plane in irregular grid pattern. Therefore, artifacts appear in the regions that violate such assumption – especially for the near-camera objects that observe *large, non-translational* motion between the source views. As can be seen from Fig. 6(d), MVSNet produces noisy outputs because the reference views from the MVLf dataset are *sparse* and with *large angular baseline*, which causes the generated feature volumes to show discontinuous costs along the depth planes, resulting in noisy disparity predictions. In addition, noisy estimations happen not only in texture-less or occlusion ambiguous regions, but in general areas with *larger* angular parallaxes. This shows that the MVSNet framework is generally unable to deal with sparse and large angular baseline source view inputs. Fig. 6(f) shows the results from our proposed method. The estimations adhere to the ground truth much better than the competing methods.

We also visually compare our results with MiDaS [35] in Fig. 7, which generates visually pleasant disparity result based on a single input RGB image. But the relative disparity scale, and the structural details within the scene are generally incorrect. This is due to its monocular pipeline, which lacks reliable geometrical clues compared with those exploited in

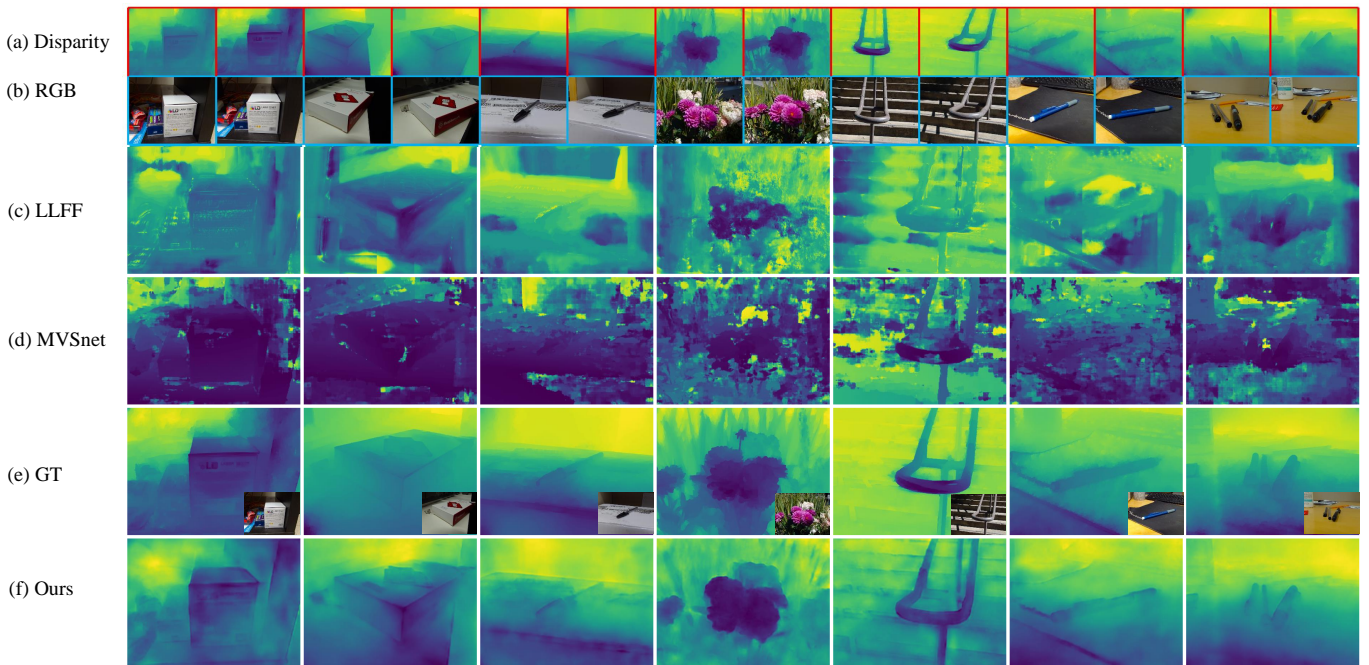


Fig. 6. Visual comparisons of predicted disparity maps between competing methods. (a) are the ground truth disparity maps from the source views (in red rectangles). (b) are the source view’s RGB images (in blue rectangles). (c) are results from LLFF (CVs) [4]. (d) are the results from MVSNet (CVs) [9]. (e) are the ground truth disparity maps calculated by using [28] and target view image (in the bottom-right corner). (f) are our results.

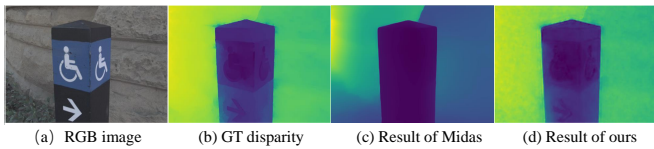


Fig. 7. Visual Comparison with MiDaS. MiDaS can generate visually pleasant disparity result as in (c). But the disparity scale, and the structural details are generally incorrect.

the multi-view frameworks.

B. Evaluation on Light Field Rendering Quality

We evaluate the quality of the final synthesized LFIs both quantitatively and qualitatively and compare with two state-of-the-art LF synthesis methods with relevant context, i.e., LLFF, which takes a group of local captures and synthesizes a local immersive LF at a given camera position via fusion of multiple multi-plane image (MPI) representations; and SynSin [13], which takes a single RGB image as input, based on which a depth map is estimated to form a point cloud representation. Point-based rendering techniques are then employed to render novel views at different angles. For both LLFF and SynSin, an immersive LF with the target image as central SAI can be synthesized by specifying the camera’s extrinsic parameters for each SAI, which we estimate based on the ground truth LFIs from the testing dataset using COLMAP.

We quantitatively evaluate the quality of the synthesized LFIs using two metrics, i.e., Peak-Signal Noise Ratio (PSNR) and Structural Similarity (SSIM), and the results are shown in TABLE VII. As can be seen, our method significantly outperforms other competing methods quantitatively by **8 dB** against LLFF, and **20 dB** against SynSin. Fig. 8 gives a qualitative presentation of the synthesized LF. We can observe

that LLFF shows poor performance over thin structures and has an aliasing effect around the object edges. SynSin suffers from noisy pixels in bright and dark regions and shows very obvious structural distortions at off-set views. Our results align much better with the ground truth both for the visual quality of the SAIs and for the linear structure preserved in the EPis, indicating that our method is able to render both spatial and angular immersive details truthfully, contributed by the high-quality disparity field estimation as well as the deep regularization modules.

C. Ablation study

Disparity Estimation Module. We carried out ablation study to evaluate the contribution of the Frustum Voxel Filtering Module and the Attention-Guided Multi-scale Residual Fusion Module for the disparity estimation.

Fig. 4 qualitatively demonstrates the contributions from these modules. We can observe significant improvements in **completeness** and **semantic correctness** in the refined disparity maps \hat{D}_{t_0} as compared with the preliminary, and initial disparity estimations D_{t_0} , D_{init} .

To quantitatively validate the respective contributions of each sub-module of the disparity estimation model, networks trained with different combinations of sub-modules are tested, and the results are presented in TABLE IV. As can be seen, without the attention units in the Attention-Guided Multi-scale Residual Fusion Module (**Ours-wo-Atten**), we observe only slight performance degradation in the metric of MSE; however, the impact is more significant on PPE. This indicates that the attention mechanism is efficient for detecting **regions with larger errors** (above the thresholds), which helps the network to focus on improving via residual fusion. When our model is

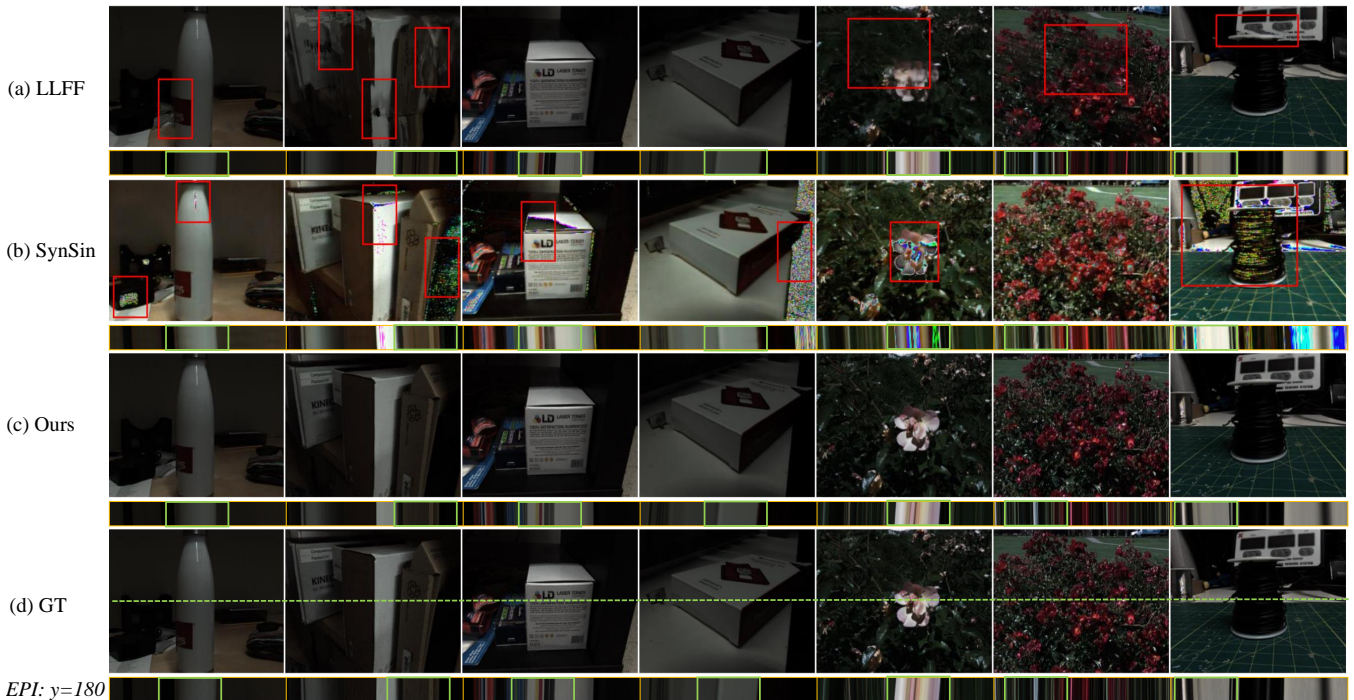


Fig. 8. Light Field synthesis visual comparison. We compare the results of our method in row (c) with those of other competing view synthesis methods, i.e., LLFF(CVs) [4] in row (a) and SynSin(CV) [13] in row (b). The ground truth SAI is in row (d). We show the top-left SAI from the 7×7 LFIs and their respective EPIs sampled at $\gamma=180$. LLFF shows poor performance on thin structures and has aliasing effect around the edges. SynSin suffers from noisy pixels in bright and dark region. Our results align much better to the ground truth both for the SAIs’ visual quality, and for the linear structure preserved in the EPIs.

TABLE IV

ABLATION STUDY ON DISPARITY ESTIMATION. THE MOST IMPORTANT FACTOR (MEASURED BY GREATEST PERFORMANCE DEGRADATION WHEN ABSENT) IS HIGHLIGHTED IN RED.

Method	Dataset Average		
Metric	MSE(px)↓	PPE(0.05, %)↑	PPE(0.1, %)↑
Ours-wo-Atten	0.063	18.826	35.528
Ours-wo-RGB	0.108	20.699	35.872
Ours	0.050	22.878	41.740

TABLE V
ABLATION STUDY ON LF SYNTHESIS.

Method	Dataset Average	
Metric	PSNR↑	SSIM↑
Ours-wo-disparity-field	30.073	0.884
Ours	33.351	0.915

without RGB image as guide (*Ours-wo-RGB*), we observe a sharp degradation in the metric of MSE. RGB is important for propagating textural and semantic information to the disparity.

Light Field Synthesis Module. The Spatial-Angular Convolution Module has been widely adopted and proven to be useful in various LF synthesis frameworks [47], [51], [52]. We only validate the functionality of disparity field estimation network by replacing it with directly copied central view’s disparity \hat{D}_{t_0} . The evaluations are conducted on LF rendering quality by calculating the PSNR and SSIM against ground truth LF L_{gt} . The results are shown in TABLE V. We can see that a performance gain of **3.278 dB** is achieved by the disparity field synthesis module.

V. CONCLUDING REMARKS

We have proposed a novel view/LF synthesis framework which robustly fuses and transfers scene geometry from large baseline LF captures. As far as we know, this is one of the first attempts for an integrated modeling scheme which transfers the requirement for a *globally-dense sampling* to a *sparse set of locally-dense sampling* (in the forms of distributed LF captures). In this sense, our work can facilitate cheap and convenient capture of target scenes. We have proposed a novel scale-consistent frustum volume rescaling algorithm which enables fusion of distributed, heterogeneous geometry embedding to be globally consistent. We have proposed novel learning-based processing modules which comprehensively regularize noisy observations from heterogeneous captures and fuse these complementary features for high-quality rendering of both disparity maps and novel LFIs. Both quantitative and qualitative experiments show that our proposed method produces precise and high-quality disparity estimation and LFIs at the target view. Our method outperforms the alternative state-of-the-art methods significantly under similar capture configurations. For future work, we plan to further explore the complementary information from different source DPVs and investigate efficient modeling mechanisms for occlusion-aware content completion and view-depend effect rendering.

REFERENCES

- [1] Paul Debevec, Yizhou Yu, and George Borshukov, “Efficient view-dependent image-based rendering with projective texture-mapping,” in *Proc. Eurographics Workshop on Rendering Techniques*, 1998, pp. 105–116.

TABLE VI

THE MSE OF DISPARITY ESTIMATION IN TEST SCENES, BEST PERFORMANCE IS HIGHLIGHTED IN RED, SECOND BEST PERFORMANCE IS HIGHLIGHTED IN BLUE. ↓ DENOTES THE SMALLER, THE BETTER.

Scene Category	Bottles	Boxes	Cacti	Flowers	Leaves	Misc	Pens	Average
Method	MSE(px)↓	MSE(px)	MSE(px)	MSE(px)	MSE(px)	MSE(px)	MSE(px)	MSE(px)
MiDaS [35] (CV)	0.217	0.402	0.127	0.246	0.284	0.554	1.086	0.444
LLFF [4] (CVs)	0.234	0.377	0.400	0.339	0.390	0.385	0.602	0.394
LLFF [4] (FCVs)	0.225	0.427	0.252	0.343	0.419	0.223	0.355	0.354
LLFF [4] (FSAIs)	0.225	0.506	0.455	0.349	0.451	0.478	0.651	0.447
MVSNet [9] (CVs)	0.342	0.382	0.360	0.370	0.450	0.416	0.432	0.399
MVSNet [9] (FCVs)	0.556	0.473	0.343	0.451	0.434	0.472	0.510	0.464
MVSNet [9] (FSAIs)	0.427	0.441	0.446	0.372	0.433	0.509	0.569	0.449
Ours	0.017	0.053	0.013	0.031	0.054	0.035	0.106	0.050

TABLE VII

LF SYNTHESIS QUALITY EVALUATION. BEST PERFORMANCE HIGHLIGHTED IN RED, SECOND BEST IN BLUE. ↑ DENOTES THE LARGER, THE BETTER.

Scene Category	Bottles	Boxes	Cacti	Flowers	Leaves	Misc	Pens	Average
Method	PSNR↑	SSIM↑	PSNR	SSIM	PSNR	SSIM	PSNR	SSIM
LLFF [4] (CVs)	31.279	0.870	30.356	0.850	20.101	0.568	22.411	0.569
LLFF [4] (FCVs)	30.608	0.878	24.110	0.728	18.259	0.446	19.480	0.394
LLFF [4] (FSAIs)	29.649	0.852	28.782	0.807	18.597	0.474	20.602	0.496
SynSin [13] (CV)	16.722	0.732	14.567	0.656	6.152	0.017	14.639	0.419
Ours	39.060	0.952	36.740	0.937	32.631	0.965	30.570	0.896

- [2] Tinghui Zhou, Richard Tucker, John Flynn, Graham Fyffe, and Noah Snavely, "Stereo magnification: Learning view synthesis using multi-plane images," *ACM Transactions on Graphics*, vol. 37, no. 4, pp. 1–12, 2018.
- [3] Jonathan Shade, Steven Gortler, Li-wei He, and Richard Szeliski, "Layered depth images," in *ACM SIGGRAPH*, 1998, pp. 231–242.
- [4] Ben Mildenhall, Pratul P. Srinivasan, Rodrigo Ortiz-Cayon, Nima Khademi Kalantari, Ravi Ramamoorthi, Ren Ng, and Abhishek Kar, "Local light field fusion: Practical view synthesis with prescriptive sampling guidelines," *ACM Transactions on Graphics*, vol. 38, no. 4, pp. 1–14, 2019.
- [5] Marc Alexa, Markus Gross, Mark Pauly, Hanspeter Pfister, Marc Stamminger, and Matthias Zwicker, "Point-based computer graphics," in *ACM SIGGRAPH*, 2004, p. 7.
- [6] Peng Dai, Yinda Zhang, Zhuwen Li, Shuaicheng Liu, and Bing Zeng, "Neural point cloud rendering via multi-plane projection," in *CVPR*, 2020, pp. 7827–7836.
- [7] Vincent Sitzmann, Justus Thies, Felix Heide, Matthias Nießner, Gordon Wetzstein, and Michael Zollhöfer, "Deepvoxels: Learning persistent 3d feature embeddings," in *CVPR*, 2019, pp. 2437–2446.
- [8] Ben Mildenhall, Pratul P. Srinivasan, Matthew Tancik, Jonathan T. Barron, Ravi Ramamoorthi, and Ren Ng, "Nerf: Representing scenes as neural radiance fields for view synthesis," in *ECCV*, 2020, pp. 405–421.
- [9] Yao Yao, Zixin Luo, Shiwei Li, Tian Fang, and Long Quan, "MVSNet: Depth inference for unstructured multi-view stereo," in *ECCV*, 2018, pp. 767–783.
- [10] Yao Yao, Zixin Luo, Shiwei Li, Tianwei Shen, Tian Fang, and Long Quan, "Recurrent MVSNet for high-resolution multi-view stereo depth inference," in *CVPR*, 2019, pp. 5525–5534.
- [11] Ren Ng, Marc Levoy, Mathieu Brédif, Gene Duval, Mark Horowitz, and Pat Hanrahan, *Light field photography with a hand-held plenoptic camera*, Ph.D. thesis, Stanford University, 2005.
- [12] Christian Perwaß and Lennart Wietzke, "Single lens 3D-camera with extended depth-of-field," *Proc. SPIE*, vol. 8291, pp. 45–59, 2012.
- [13] Olivia Wiles, Georgia Gkioxari, Richard Szeliski, and Justin Johnson, "SynSin: End-to-end view synthesis from a single image," in *CVPR*, 2020, pp. 7465–7475.
- [14] Nima Khademi Kalantari, Ting-Chun Wang, and Ravi Ramamoorthi, "Learning-based view synthesis for light field cameras," *ACM Transactions on Graphics*, vol. 35, no. 6, pp. 1–10, 2016.
- [15] Inchang Choi, Orazio Gallo, Alejandro Troccoli, Min H Kim, and Jan Kautz, "Extreme view synthesis," in *ICCV*, 2019, pp. 7781–7790.
- [16] Jing Jin, Junhui Hou, Jie Chen, Huanqiang Zeng, Sam Kwong, and Jingyi Yu, "Deep coarse-to-fine dense light field reconstruction with flexible sampling and geometry-aware fusion," *IEEE Transactions on Pattern Analysis and Machine Intelligence*, pp. 1–1, 2020.
- [17] Pratul P. Srinivasan, Richard Tucker, Jonathan T. Barron, Ravi Ramamoorthi, Ren Ng, and Noah Snavely, "Pushing the boundaries of view extrapolation with multiplane images," in *CVPR*, 2019, pp. 175–184.
- [18] Richard Hartley and Andrew Zisserman, *Multiple View Geometry in Computer Vision*, Cambridge University Press, 2 edition, 2004.
- [19] Richard A Newcombe, Steven J Lovegrove, and Andrew J Davison, "DTAM: Dense tracking and mapping in real-time," in *ICCV*, 2011, pp. 2320–2327.
- [20] Matia Pizzoli, Christian Forster, and Davide Scaramuzza, "REMODE: Probabilistic, monocular dense reconstruction in real time," in *IJCV*, 2014, pp. 2609–2616.
- [21] Johannes Lutz Schönberger and Jan-Michael Frahm, "Structure-from-motion revisited," in *CVPR*, 2016, pp. 4104–4113.
- [22] Jiayu Yang, Wei Mao, Jose M. Alvarez, and Miaomiao Liu, "Cost volume pyramid based depth inference for multi-view stereo," in *CVPR*, 2020, pp. 4876–4885.
- [23] Rui Chen, Songfang Han, Jing Xu, and Hao Su, "Point-based multi-view stereo network," in *ICCV*, 2019, pp. 1538–1547.
- [24] Zehao Yu and Shenghua Gao, "Fast-mvsnet: Sparse-to-dense multi-view stereo with learned propagation and gauss-newton refinement," in *CVPR*, 2020, pp. 1949–1958.
- [25] Sven Wanner and Bastian Goldluecke, "Globally consistent depth labeling of 4D light fields," in *CVPR*, 2012, pp. 41–48.
- [26] Changil Kim, Henning Zimmer, Yael Pritch, Alexander Sorkine-Hornung, and Markus Gross, "Scene reconstruction from high spatio-angular resolution light fields," *ACM Transactions on Graphics*, vol. 32, no. 4, pp. 73:1–73:12, 2013.
- [27] Ting Chun Wang, Alexei A. Efros, and Ravi Ramamoorthi, "Occlusion-aware depth estimation using light-field cameras," in *ICCV*, 2016, pp. 3487–3495.
- [28] Jie Chen, Junhui Hou, Yun Ni, and Lap-Pui Chau, "Accurate light field depth estimation with superpixel regularization over partially occluded regions," *IEEE Transactions on Image Processing*, vol. 27, no. 10, pp. 4889–4900, 2018.
- [29] Hae Gon Jeon, Jaesik Park, Gyeongmin Choe, Jinsun Park, Yunsu Bok, Yu Wing Tai, and In So Kweon, "Accurate depth map estimation from a lenslet light field camera," in *CVPR*, 2015, pp. 1547–1555.
- [30] Stefan Heber, Wei Yu, and Thomas Pock, "Neural epi-volume networks for shape from light field," in *ICCV*, 2017, pp. 2271–2279.
- [31] Jiayong Peng, Zhiwei Xiong, Dong Liu, and Xuejin Chen, "Unsupervised depth estimation from light field using a convolutional neural network," in *International Conference on 3D Vision*, 2018, pp. 295–303.
- [32] Changha Shin, Hae-Gon Jeon, Youngjin Yoon, In So Kweon, and Seon Joo Kim, "Epinet: A fully-convolutional neural network using epipolar geometry for depth from light field images," in *CVPR*, 2018, pp. 4748–4757.
- [33] Chunle Guo, Jing Jin, Junhui Hou, and Jie Chen, "Accurate light field depth estimation via an occlusion-aware network," in *ICME*, 2020, pp. 1–6.
- [34] Moritz Menze and Andreas Geiger, "Object scene flow for autonomous vehicles," in *CVPR*, 2015, pp. 3061–3070.
- [35] René Ranftl, Katrin Lasinger, David Hafner, Konrad Schindler, and Vladlen Koltun, "Towards robust monocular depth estimation: Mixing

- datasets for zero-shot cross-dataset transfer,” *IEEE Transactions on Pattern Analysis and Machine Intelligence*, p. 1, 2020.
- [36] John Flynn, Michael Broxton, Paul Debevec, Matthew DuVall, Graham Fyffe, Ryan Overbeck, Noah Snavely, and Richard Tucker, “Deepview: View synthesis with learned gradient descent,” in *CVPR*, 2019, pp. 2367–2376.
- [37] Jeong Park, Peter Florence, Julian Straub, Richard Newcombe, and Steven Lovegrove, “Deepsdf: Learning continuous signed distance functions for shape representation,” in *CVPR*, 2019, pp. 165–174.
- [38] Chiyu Jiang, Avneesh Sud, Ameesh Makadia, Jingwei Huang, Matthias Nießner, and Thomas Funkhouser, “Local implicit grid representations for 3D scenes,” in *CVPR*, 2020, pp. 6000–6009.
- [39] Kyle Genova, Forrester Cole, Avneesh Sud, Aaron Sarna, and Thomas Funkhouser, “Local deep implicit functions for 3D shape,” in *CVPR*, 2020, pp. 4857–4866.
- [40] Leif Kobbelt and Mario Botsch, “A survey of point-based techniques in computer graphics,” *Computer Graphics*, vol. 28, no. 6, pp. 801–814, 2004.
- [41] Moustafa Meshry, Dan B. Goldman, Sameh Khamis, Hugues Hoppe, Rohit Pandey, Noah Snavely, and Ricardo Martin-Brualla, “Neural rerendering in the wild,” in *CVPR*, 2019, pp. 6871–6880.
- [42] A. Kubota, K. Aizawa, and T. Chen, “Reconstructing dense light field from array of multifocus images for novel view synthesis,” *IEEE Transactions on Image Processing*, vol. 16, no. 1, pp. 269–279, 2007.
- [43] Fitzgibbon, Wexler, and Zisserman, “Image-based rendering using image-based priors,” in *ICCV*, 2003, pp. 1176–1183.
- [44] Lixin Shi, Haitham Hassanieh, Abe Davis, Dina Katabi, and Fredo Durand, “Light field reconstruction using sparsity in the continuous fourier domain,” *ACM Transactions on Graphics*, vol. 34, no. 1, pp. 1–13, 2015.
- [45] S. Vagharshakyan, R. Bregovic, and A. Gotchev, “Light field reconstruction using shearlet transform,” *IEEE Transactions on Pattern Analysis and Machine Intelligence*, vol. 40, no. 1, pp. 133–147, 2018.
- [46] Pratul P Srinivasan, Tongzhou Wang, Ashwin Sreelal, Ravi Ramamoorthi, and Ren Ng, “Learning to synthesize a 4D RGBD light field from a single image,” in *ICCV*, 2017, pp. 2243–2251.
- [47] Henry Wing Fung Yeung, Junhui Hou, Jie Chen, Yuk Ying Chung, and Xiaoming Chen, “Fast light field reconstruction with deep coarse-to-fine modeling of spatial-angular clues,” in *ECCV*, 2018, pp. 137–152.
- [48] G. Wu, M. Zhao, L. Wang, Q. Dai, T. Chai, and Y. Liu, “Light field reconstruction using deep convolutional network on epi,” in *CVPR*, 2017, pp. 1638–1646.
- [49] Johannes Lutz Schönberger, Enliang Zheng, Marc Pollefeys, and Jan-Michael Frahm, “Pixelwise view selection for unstructured multi-view stereo,” in *ECCV*, 2016, pp. 501–518.
- [50] Dhruv Kumar Mahajan, Ross B. Girshick, Vignesh Ramanathan, Kaiming He, Manohar Paluri, Yixuan Li, Ashwin Bharambe, and Laurens van der Maaten, “Exploring the limits of weakly supervised pretraining,” in *ECCV*, 2018, pp. 181–196.
- [51] H. W. F. Yeung, J. Hou, X. Chen, J. Chen, Z. Chen, and Y. Y. Chung, “Light field spatial super-resolution using deep efficient spatial-angular separable convolution,” *IEEE Transactions on Image Processing*, vol. 28, no. 5, pp. 2319–2330, 2019.
- [52] Henry Yeung, Junhui Hou, Xiaoming Chen, Jie Chen, Zhibo Chen, and Yuk Chung, “Light field spatial super-resolution using deep efficient spatial-angular separable convolution,” *IEEE Transactions on Image Processing*, vol. 28, no. 5, pp. 2319–2330, 2018.
- [53] Donald G. Dansereau, Bernd Girod, and Gordon Wetzstein, “Liff: Light field features in scale and depth,” in *CVPR*, 2019, pp. 8034–8043.
- [54] Matthew D Zeiler, “Adadelta: an adaptive learning rate method,” *arXiv preprint arXiv:1212.5701*, 2012.